J. Fluid Mech. (2009), *vol.* 634, *pp.* 41–60. © 2009 Cambridge University Press
doi:10.1017/S0022112009007745 Printed in the United Kingdom

Dynamics of passive scalars and tracers advected by a two-dimensional tripolar vortex

PAULO J. S. A. FERREIRA DE SOUSA[1,2]† AND JOSÉ C. F. PEREIRA[2]

[1]Department of Mechanical and Aerospace Engineering, New Mexico State University,
Las Cruces, NM 88003, USA

[2]Department of Mechanical Engineering/LASEF, Instituto Superior Técnico (IST),
Av. Rovisco Pais 1, 1049-001 Lisboa, Portugal

(Received 7 February 2007 and in revised form 16 April 2009)

The dynamics of passive scalars and tracers during the formation and subsequent persistence of a laminar tripolar vortex, obtained through an unstable monopolar vortex seeded with a $k=2$ azimuthal perturbation, is investigated. Two-dimensional direct numerical simulations of passive scalars with Schmidt numbers $Sc=0.1$, 1, 10 and 100 are performed. The scalar variance for the four cases is analysed, as well as the different dispersion patterns up to 10 times greater than the time for formation of the tripolar vortex. During the formation of the tripole, an accelerated scalar dissipation is observed. That dissipation is connected to the advection-dominated processes associated with the growth of the perturbation mode. During that process, the patterns of mixing of the different passive scalars are very much the same as for vorticity. This stage of accelerated dissipation is preceded and followed by stages of diffusion-dominated scalar dissipation. Passive Lagrangian tracers are used to explore the transport of fluid elements during the evolution, and to provide a detailed view of the tripolar vortex formation and behaviour for longer times. Chaotic mixing was studied by examining patterns of spatial variation of finite-time Lyapunov exponents. As the perturbation grows and the tripolar vortex is formed, two large regions of regular flow, divided by a region of chaotic flow, form for each satellite. When the tripole is fully formed, it is composed of three distinct regular regions, corresponding to the core of negative vorticity and the two satellites of positive vorticity. The comparison between the evolution for vorticity, concentration, randomly distributed particles and Lyapunov exponents shows that transport occurs mainly in the regions of chaotic flow that surround the tripolar vortex after its formation. For longer times, both the chaotic/regular flow interfaces and the vorticity gradients are responsible for the integrity of the tripolar system.

1. Introduction

The dispersion of passive scalars in a given velocity field is the result, usually highly non-trivial, of two different contributions: molecular diffusion and advection. The problem of how fluid motion and molecular diffusion interact in order to accelerate transport has been explored for many applications. For passive scalars, the small-scale structure is influenced, besides the Reynolds number, by the Schmidt number

† Email address for correspondence: ferreiradesousa@gmail.com

$Sc = \nu/\kappa$, where ν is the kinematic viscosity of the fluid and κ is the molecular diffusivity of the scalar. The Schmidt number can vary widely in applications, from order 10^{-3} in liquid metals to order unity in gaseous flames to thousands and higher in organic mixtures and biological fluids. In oceanographic applications temperature and salinity are important scalars and both have $Sc > 1$.

The investigation of passive scalar advection and diffusion in two-dimensional flows has received a wide range of interest, ranging from some problems of fluid turbulence (see Babiano et al. 1987; Bogucki, Domaradzki & Yeung 1997; Warhaft 2000) to its direct applicability to physical problems arising in laboratory experiments and/or in nature. Examples of such problems are some stably stratified flows in the stratosphere or ocean that can be considered almost planar flows.

In this paper we want to investigate the advection and diffusion of a passive scalar $\theta(\mathbf{x}, t)$ in a two-dimensional, incompressible, time-dependent, perturbed vortical flow, a tripole. In forced two-dimensional turbulence, Legras, Santangelo & Benzi (1988) observed a complex coherent compound vortex, the tripole, which is characterized by an elliptic vortex surrounded by two satellite vorticity patches rotating in the opposite direction. The formation of tripoles from unstable monopolar vortices was predicted by Leith (1984) and verified later in experiments with rotating fluids (van Heijst & Kloosterzil 1989; van Heijst, Kloosterziel & Williams (1991); Fuentes, van Heijst & van Lipzig 1996), as well as in numerical work by Carton, Flierl & Polvani (1989). The cited laboratory experiments and numerical simulations showed that tripole formation is the result of an azimuthal wavenumber-2 instability of an unstable isolated circular vortex. Rossi, Lingevitch & Bernoff (1997) determined that there is a threshold amplitude above which a perturbed Gaussian monopole will relax to a quasi-steady rotating tripole, and below which will relax to an axisymmetric monopole. The resulting quasi-steady structures are robust to small perturbations, which accounts for the remarkable stability that tripoles have, in the sense that they survive many rotations of the system. However, in the case when they are generated off-axis they change very quickly. A tripolar structure, consisting of an anti-cyclonic core and two cyclonic satellites, with a period of rotation of 18 days and characteristic dimensions of about 50–70 km, was visible in the sea of the Bay of Biscay during the period May 1991 to February 1992 (Pingree & LeCann 1992). Similar structures in plasmas were predicted from the theory of electromagnetic drift waves in plasmas with magnetic shear and in a shallow atmosphere (Vranjes 1999; Vranjes, Stenflo & Shukla 1999*b*). Tripoles were also predicted in the presence of low-frequency dust-drift waves in a non-uniform dusty plasma with a sheared flow (Vranjes, Maric & Shukla 1999*a*). From the vorticity contour plots of Kloosterziel & Carnevale (1999) as well as from Ferreira de Sousa & Pereira (2005), it can be seen that for later times the vorticity filaments that originate at the tripole formation seem to persist and roll up into secondary vortices.

The consideration of the dynamics of Lagrangian tracers allows better characterizing of the core dynamics and determining the regions of the fluid entrained in the final vortex core. Passive particle dynamics is also valuable for qualitatively comparing with the scalar concentration patterns. The study of passive scalar advection and diffusion in two-dimensional vortical structures was conducted by Rhines & Young (1983) that showed that a scalar placed inside a single vortex decays quickly along the streamlines of the flow, and diffusion occurs in a much slower time frame in a direction perpendicular to the streamlines. The quick decay of the scalar is caused by the shear in differential rotation and molecular diffusion. Flohr & Vassilicos (1997) showed that there is an accelerated scalar dissipation in an isolated vortex by studying the evolution of a scalar patch that evolves into a spiral structure as it wraps around a steady vortex. The response of a Gaussian vortex to an impulsive strain was numerically studied, first for the linear case (Bassom & Gilbert 1998), and for the nonlinear case (Bassom & Gilbert 1999) for inviscid flow. The latter study also studies the response of a Gaussian vortex to a step function and a random function of time. This subject was further studied by Bajer, Bassom & Gilbert (2001) that considered the spiral wind-up and diffusive decay of a passive scalar in circular streamlines. Wonhas & Vassilicos (2001) investigated passive scalar advection–diffusion in frozen two-dimensional non-circular symmetric vortices and identified three different regions with different mixing properties. The advection of a passive scalar patch in the deformation field of an axisymmetric Gaussian vortex was experimentally studied by Meunier & Villermaux (2003). The patch initially rolls up in a spiral and then fades away in the solution. The probability density function of the concentration levels is analysed and it is shown that there is a direct connection between the microscopic equations of diffusion and the resulting global statistics of the mixture.

Lagrangian motions associated with coherent vortices have long been studied in the context of geophysical fluid dynamics (for a review see Provenzale 1999). In von Hardenberg *et al.* (2000), passive Lagrangian tracers are used to study symmetric vortex merger in quasi-geostrophic flows using numerical simulations. The use of Lagrangian tracers provides a detailed view of the flow evolution, and to determine the value of the critical merging distance for baroclinic vortices. A way to identify and characterize the chaotic regions of a flow is to look into the spatial distribution of the finite-time Lyapunov exponents (FTLEs). This was first done by Pierrehumbert (1991) in the context of horizontal mixing in planetary atmospheres and further extended to two-dimensional mixing on isentropic surfaces in the troposphere in Pierrehumbert & Yang (1993). The dynamics of a passive tracer was also investigated in the velocity field of three (Kuznetsov & Zaslavsky 1998; Kuznetsov & Zaslavsky 2000) and four identical point vortices, Boatto & Pierrehumbert (1999). In the last decade, more interest has been given to Lagrangian motions in the context of turbulent flows (for a review see Yeung 2002). Lapeyre (2002) applied Lyapunov theory in chaotic systems to the dynamics of tracer gradients in the context of two-dimensional turbulence. Other applications of FTLEs include real atmospheric flows (see e.g. Abraham & Bowen 2002; Waugh, Abraham & Bowen 2006).

The objective of this paper is to study passive scalar advection and diffusion by both Eulerian and Lagrangian methods, in a two-dimensional flow with physical significance: the tripole. By investigating the scalar evolution for four different Schmidt numbers we can access the effect of this parameter spanning three orders of magnitude. By analysing the kinematics of passive tracers, we obtain further insight on the time dependent stirring characteristics of a transient two-dimensional realistic flow.

In the next section of this paper, we present the numerical model employed to solve the two-dimensional unsteady incompressible Navier–Stokes equations, including the transport equation for a passive scalar. This is followed by the presentation of the results grouped into two sections. First, the scalar variance of passive scalars is calculated and the various stages of mixing of the scalars are identified. The scalar concentration spatial distributions for the evolution of the studied vortex is analysed as well for three of the Schmidt numbers calculated. Second, a characterization of the evolution was done in a Lagrangian framework by analysing the dynamics of particles with vanishing inertia. This was done first by placing randomly distributed particles in two regions that define the core of the initial circular vortex and analysing the evolution of the clouds of tracers that formed. Then the degree of chaos of the flow was measured by investigating the evolution of the Lyapunov exponents for a Cartesian grid of particles.

2. Numerical method

2.1. *Navier–Stokes equations*

The flow dynamics are described by the incompressible Navier–Stokes equations for velocity $\boldsymbol{u}$:

$$\nabla \cdot \boldsymbol{u} = 0, \tag{2.1}$$

$$\frac{\partial \boldsymbol{u}}{\partial t} + (\boldsymbol{u} \cdot \nabla)\boldsymbol{u} = \nu \nabla^2 \boldsymbol{u} - \nabla p. \tag{2.2}$$

In the equations p denotes the pressure that is divided by density and ν the kinematic viscosity of the fluid.

The momentum equations are spatially discretized on a staggered mesh by finite differences and all derivatives are evaluated with implicit 10th-order compact finite difference schemes (Lele 1992). The fourth-order accurate Runge–Kutta scheme was used for temporal discretization. Periodic boundary conditions were applied to all discrete operators used.

The numerical method used belongs to the projection methods class, which are based on the Helmholtz–Hodge decomposition theorem and the resulting Poisson equation was also discretized with compact operators, the procedure is presented in Ferreira de Sousa & Pereira (2005).

In this paper we seek solutions of the transport equation for the passive scalar $\theta(\mathbf{x}, t)$:

$$\frac{\partial}{\partial t}\theta + \boldsymbol{u} \cdot \nabla \theta = \kappa \nabla^2 \theta. \tag{2.3}$$

In order to solve (2.3), time was advanced using the fourth-order accurate Runge–Kutta scheme similar to the one used to explicitly solve the momentum equations.

For all calculations the computational domain extends to 10 non-dimensional units for each coordinate direction. This was discretized by a mesh comprising 256×256 nodes. Time was scaled by $|\omega(0)|^{-1}$ and the time step used was 5×10^{-2}, corresponding to a Courant–Friedrichs–Lewy (CFL) number of 1.28. The kinematic viscosity was set to $\nu = 1 \times 10^{-5}\ \mathrm{m^2\,s^{-1}}$.

3. Results

The formation of a tripole has been extensively studied. Kloosterziel & Carnevale (1999) have investigated numerically the stability of circular vortices with a radial vorticity given by

$$\overline{\omega}_\alpha(r) = \left(\frac{1}{2}\alpha r^\alpha - 1\right)\exp(-r^\alpha). \tag{3.1}$$

The vorticity is negative near the centre and positive further out. The corresponding velocity profiles $\overline{v}_\alpha(r) = -r\exp(-r^\alpha)/2$ increase from zero at $r = 0$ to a maximum at $r = (1/\alpha)^{(1/\alpha)}$, falling monotonically to zero. The flow is everywhere clockwise.

For small-enough positive α these vortices are linearly stable. For approximately $\alpha > 1.85$ they become unstable to perturbations with $k = 2$. For approximately $\alpha > 3$ they first become unstable to $k = 3$ and for $\alpha > 4$ they become unstable to wavenumber-4 instabilities (Kloosterziel & Carnevale 1999).

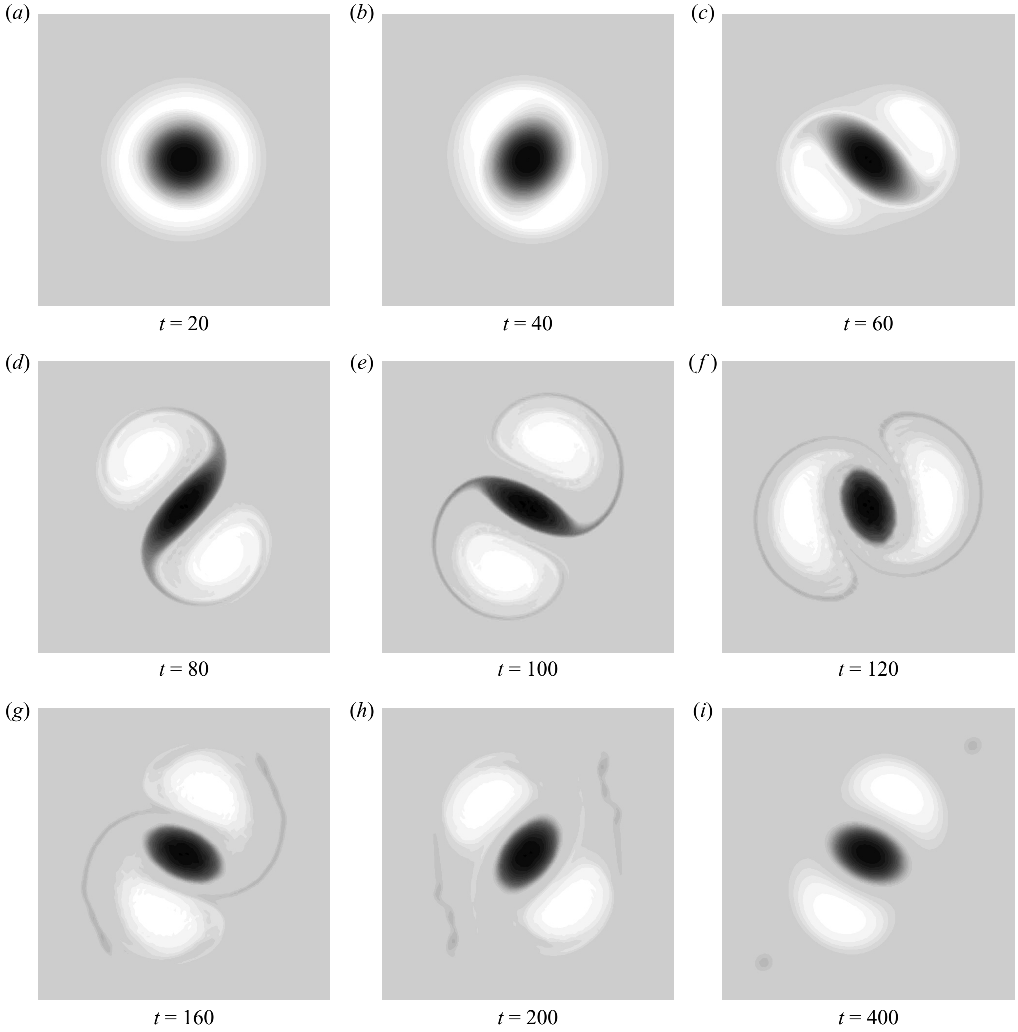

FIGURE 1. Contour plots of vorticity for a $\overline{\omega}_{\alpha=3}$ vortex initially perturbed with a perturbation of type (3.2) with $k = 2$, $\mu = 0.1$, $\sigma = 0.25$.

In order to excite instabilities, the following initial vorticity perturbation was used

$$\omega' = \mu \cos(k\theta) \exp\left[\frac{-(\sigma r^{\alpha} - 2)}{2\sigma^2}\right], \tag{3.2}$$

where μ and σ are constants and k is an azimuthal wavenumber.

Figure 1 shows the predicted evolution of the distribution of vorticity for the $\alpha = 3$ vortex flow with a $k = 2$ perturbation given by (3.2). For this vortex the only unstable normal mode is $k = 2$.

Figure 1(*a*) shows the initial vorticity distribution that is composed of a core of negative vorticity, surrounded by a ring of positive vorticity. The seeded perturbation goes on to grow with an exponential rate as predicted by linear dynamics, that is halted due to nonlinear effects. The growth of the perturbation mode causes the core to become deformed. At $t = 40$, figure 1(*b*), the vortex core is already exhibiting an elliptical shape. As the core of negative vorticity goes through further deformation, it breaks through the ring of positive vorticity for $50 < t < 60$. In figure 1(*d*), at $t = 80$, two satellites, semi-circular areas of positive vorticity, have formed while weak negative vorticity filaments start to wrap around the satellites. At the same time, the core reaches its maximum ellipticity. From $t = 80$ to $t = 120$ the core almost returns to a circular shape, which causes the filaments of negative vorticity to break off from the core. From then on the core goes through periodic cycles of elongation that are slowly dampened. The broken off filaments evolve into isolated vorticity filaments that stay more or less stationary outside the tripole, visible for $t = 200$. These vorticity filaments are unstable and roll up forming new vortical structures. The stability of these filaments depends on the rate of strain associated with the vorticity field of the tripole and the local vorticity of the filament. When the vortex-induced strain dominates, the filament is stable. On the contrary, when the local vorticity of the filament dominates, the filament becomes unstable and rolls up, forming new vortices (Kevlahan & Farge 1997; Elhmaidi *et al.* 2004). These secondary vortices are an integral part of the system associated with the tripole and persist for larger times (figure 1*i*). It should be pointed out that in the stationary frame of reference, which is the one pictured, the secondary vortices do not stay in the exact same place, they move outwards/inwards as the poles of positive vorticity pass them. The peak of vorticity of the secondary vortices for $t = 1000$ is approximately $\omega = -0.08$. Similar calculations (not shown) were done using a randomly perturbed $\alpha = 3$ vortex. These calculations show that the evolution pictured here is not dependent on the nature of the initial perturbation. When randomly perturbed, a $\alpha = 3$ vortex develops the same $k = 2$ perturbation and the same tripolar vortex is formed.

3.1. *Scalar variance in a vortex*

We are interested in a description of the mixing process and one measure for mixing is the scalar variance. The decay of the scalar can be calculated by

$$\Delta E_\theta(t) = \overline{\theta^2}(0) - \overline{\theta^2}(t), \tag{3.3}$$

where the scalar variance $\overline{\theta^2}(t)$ is defined by

$$\overline{\theta^2}(t) = \int |\theta(x, y, t)|^2 \,\mathrm{d}x\,\mathrm{d}y. \tag{3.4}$$

Unlike the spatial mean of a scalar, the variance is a non-conserved quantity. It decays during the advection–diffusion process and is a measure of how evenly the scalar is distributed in space. Its lowest value is reached when the scalar is uniformly distributed in space.

Figure 2 shows the evolution of the scalar variance $\Delta E_\theta(t)$ for Schmidt numbers $Sc = 0.1$, 1, 10 and 100. From the immediate analysis of the plot we can identify three different regimes of dissipation of the scalar. The first region is a purely diffusive stage that occurs before the growth of the perturbation mode and is not influenced by the dynamics of the formation of the tripole. The slope of the variance for this stage varies with the Schmidt number, even though for early times it approaches the theoretical prediction, $\Delta E_\theta(t) \sim t^{1/2}$.

The second stage, that begins after $t = 60$ and occurs slightly later for decreasing Sc numbers, is characterized by an accelerated scalar dissipation and marked by the formation of the tripole, since it occurs at the same time as the vortex core breaks through the ring of positive vorticity and starts to wrap around the two satellites. This stage ends around $t = 120$ for all Schmidt numbers.

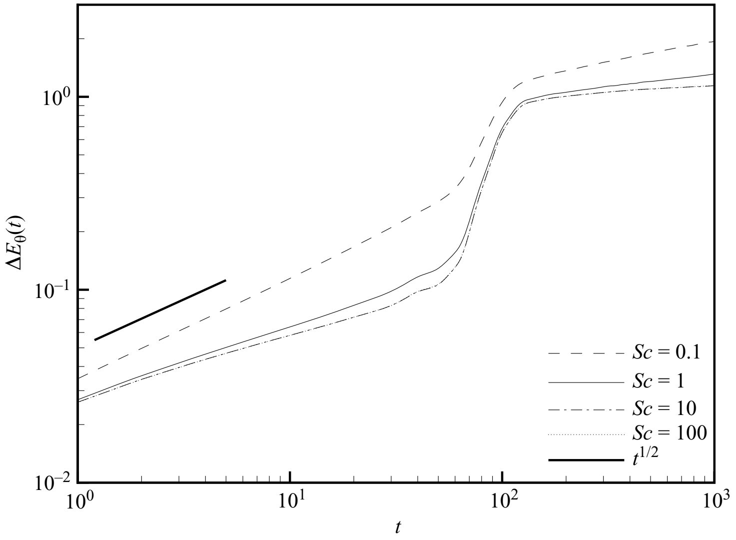

FIGURE 2. Evolution of the scalar variance for four different Schmidt numbers. The curves for $Sc = 10$ and $Sc = 100$ are indistinguishable.

A third stage can be identified after the tripole formation which is again strongly driven by diffusion. However, for this second diffusive stage, the slope of the scalar variance evolution is different than the one before the tripole formation, with the scalar variance $\Delta E_\theta(t)$ increasing at a lower slope for increasing Schmidt number.

Even though there is a marked influence of the Schmidt number on the evolution of the scalar variance throughout the process of the tripole formation, that influence is not apparent for larger values of this parameter. For Sc numbers larger than 10, there is little difference for the evolution of the scalar variance. This is due to the fact that for $Sc = 10$ the characteristic time scale for the diffusion of the scalar can be regarded as already very large compared to the characteristic time scale of the vortex evolution.

In the simulations presented here, Schmidt numbers of $Sc \leqslant 100$ have been used, but in fact, and as an example, the diffusivity of salt in water is characterized by a much larger Schmidt number: $Sc \approx 700$. In general it is difficult to perform well resolved simulations for realistic values of the Schmidt number, particularly for high Reynolds numbers. The results shown in figure 2 indicate that it is reasonable to perform numerical simulations with $Sc = 10$, without changing the flow dynamics compared to real conditions.

3.2. *Scalar concentration distribution*

The temporal evolution of the concentration of scalars with different Schmidt numbers is useful as it shows the mixing patterns that can be related to a variety of passive scalars in a flow, e.g. pollutants or non-reacting chemicals. Also the visualization of patterns of scalar concentration can be closely related to and compared to experimental dye visualizations. If a passive scalar blob such as dye or temperature is placed in a smooth planar vortex, the scalar becomes wound up into a spiral structure because of differential rotation. Although the wind-up of vorticity and scalar look very similar, there are a number of differences because the vorticity is coupled back to the flow field.

The trapping properties of coherent vortices can be understood by noting that the vortices have a strong vorticity gradient at their edge, which separates the rotation-dominated core from the strain dominated region just outside. This is also true for the initial monopole that originates the tripole, as the vorticity distribution of a monopole is characterized by a core of one sign of vorticity, surrounded by a ring of oppositely signed vorticity. Regions of uniform or gently variable vorticity are easily crossed by fluid particles while regions of large vorticity gradient act as transport barriers. The edge of a coherent vortex may thus be defined as the isoline of maximum vorticity gradient closer to the vortex centre (Provenzale 1999). Because for the vortices defined by (3.1) that isoline is very close to the line for $\omega = 0$, we choose to use the latter to define the initial core edge of concentration. Both of these definitions provide consistent definitions of the vortex edge.

Figure 3 shows the evolution of the concentration for a passive scalar with $Sc = 1$. For $t = 0$ (not shown), the concentration distribution consists of a circular patch where concentration is equal to 1 in the area of negative vorticity and 0 elsewhere. At $t = 40$ (figure 3*b*) the patch of scalar concentration starts to be deformed and assumes an elliptical shape, following the shape of the region of negative vorticity. However, some scalar dissipation occurs at the edge of the patch due to diffusion. For $t = 60$, filaments of scalar concentration start to wrap around the satellites. This coincides with the beginning of the stage of accelerated scalar dissipation. As the core of negative vorticity breaks through the ring of positive vorticity, and due to the overall rotation of the vortex system, scalar concentration filaments wrap around the two satellites. In this process, the passive scalar has a similar behaviour to the weak vorticity contained in these filaments. The time frame of accelerated scalar dissipation, which roughly occurs between $t = 60$ and $t = 120$ coincides with the maximum ellipticity of the core and the formation of the filaments of scalar concentration. With the maximum ellipticity of the core, around $t = 80$, the accelerated scalar dissipation is at its highest rate. After the peak of ellipticity of the core, it returns to a more circular shape. As the core goes through this cycle, the scalar concentration filaments break off from the core and the stage of accelerated scalar dissipation is over. The positive vorticity satellites are engulfed by closed filaments of scalar concentration. In figure 3(*f*), for $t = 120$, the core is returning to a circular shape and the remainder of the filaments start to form a patch of scalar concentration that can be seen for $t = 160$ and persists in the 2 and 8 o'clock regions around the tripole, following the evolution of the weak vorticity filaments in that region. For this set of results, the scalar concentration of the positive vorticity satellites remains zero, meaning that the scalar does not diffuse into this region, closely following the regions of negative vorticity. Figures 3(*i*)–3(*l*) document the evolution of the scalar concentration for $Sc = 1$ for later times. After the evolutions described above that occur for $t \leqslant 200$, the scalar filaments follow the path of the weak vorticity filaments, eventually forming circular scalar concentration islands. So for later times we have two small islands of scalar concentration in the 2 and 8 o'clock regions around the tripole. The concentration in these islands is around 20 % for $t = 1000$.

Because the tripole formation is an advection-driven process, the scalar concentration patterns are not very different for the three Schmidt numbers. The differences occur mainly for the scalar concentration gradient, which is better preserved for the results with a higher Schmidt number, with the results for lower molecular diffusivity showing a significant diffusion in the edge of the core. Figure 4 compares the scalar concentration contour plots at $t = 120$. For this time, the accelerated dissipation stage has ended, and the diffusive processes have clearly

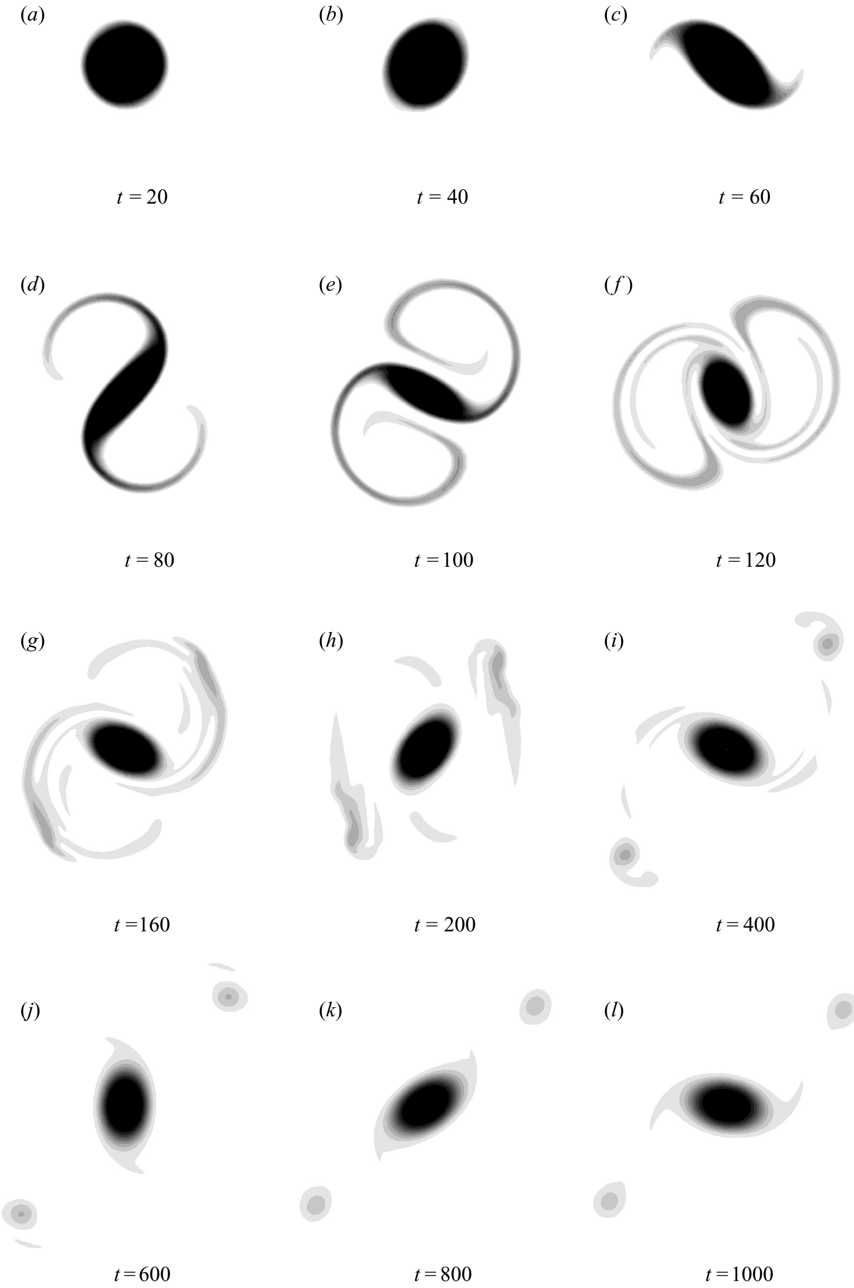

FIGURE 3. Scalar concentration distribution. Black is for $\theta = 1$ and white for $\theta = 0$. $Sc = 1$.

taken over, meaning that the scalar concentration decays more quickly for $Sc = 0.1$, as expected. The effect of the Schmidt number, and thus molecular diffusivity, is marked. As the accelerated dissipation stage ends, the evolution of the scalar concentration patterns are once again governed by diffusion. The effect of scalar diffusion is

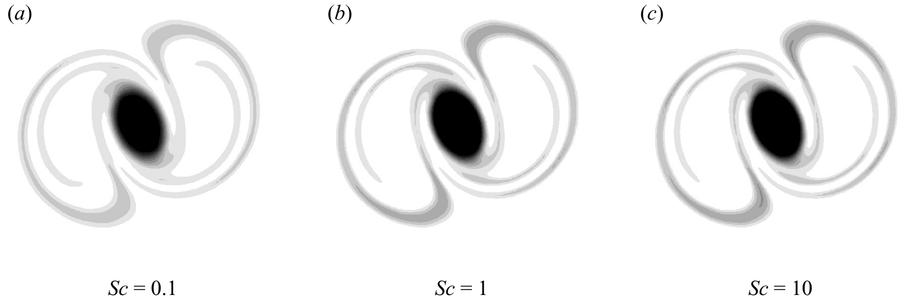

FIGURE 4. Scalar concentration distribution for $t = 120$.

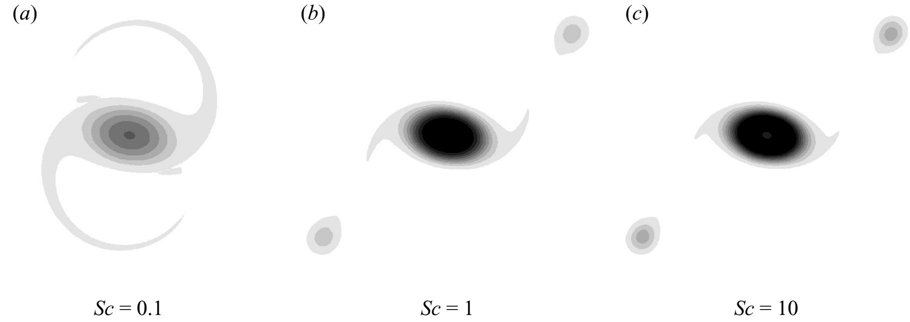

FIGURE 5. Scalar concentration distribution for $t = 1000$.

highlighted when we compare the scalar concentration contour plots for the end of the simulation, $t = 1000$ (figure 5). It should be noted that even for the results with lower Schmidt number, the concentration inside the satellites of positive vorticity stays close to zero. As for the secondary scalar islands at 2 and 8 o'clock, their peak concentration is quite significant for $Sc = 10$, around 27 %. The concentrations for $Sc = 1$ and 0.1 are 20 % and 6 %, respectively.

3.3. *Lagrangian analysis*

In the previous section the characterization of the evolution was done in a standard Eulerian framework. The dynamics of fluid particles during the evolution of the tripole provides a complimentary Lagrangian picture of the process.

The equations of motion for passive, point-like Lagrangian particles having vanishing inertia with respect to the advecting fluid are obtained by equating the Lagrangian velocity $\boldsymbol{V}(t)$ to the Eulerian velocity $\boldsymbol{u}(\boldsymbol{x}, t)$ at the particle position

$$\frac{\mathrm{d}\boldsymbol{x}}{\mathrm{d}t} = \boldsymbol{V}(t) = \boldsymbol{u}(\boldsymbol{x}, t). \tag{3.5}$$

For two-dimensional incompressible flows, such as those discussed in the previous section, the Eulerian velocity may be expressed in terms of a stream function $\psi(x, y, t)$. In this case, (3.5) becomes

$$\frac{\mathrm{d}x}{\mathrm{d}t} = -\frac{\partial \psi}{\partial y}, \quad \frac{\mathrm{d}y}{\mathrm{d}t} = \frac{\partial \psi}{\partial x}. \tag{3.6}$$

Equation (3.6) formally defines a Hamiltonian system with one degree of freedom, described by the canonically conjugate variables x and y. Here, the stream function plays the role of the Hamiltonian and the phase space of the system is the physical plane (x, y) (see e.g. Ottino 1990). For stationary stream functions, (3.6) is integrable, the particles follow the streamlines, and all particle trajectories are regular. When the stream function is time-dependent, the system becomes non-integrable. In this case, chaotic particle trajectories are expected and the Lagrangian motion may become highly irregular even if the Eulerian dynamics is simple. This type of behaviour, known as chaotic advection, has been studied by many authors (see e.g. the review by Ottino 1990).

In order to obtain the tracer dynamics, the numerical integration is done through a Runge–Kutta fourth-order scheme and a local interpolator based on spline interpolation is used to obtain the velocity at the tracer position.

3.3.1. *Lagrangian picture of the evolution*

Lagragian tracers provide a detailed picture of the evolution of the vortex core during the tripole formation. To obtain the Lagrangian picture of the flow evolution, we randomly distribute 32 768 passive particles in two different regions of the initial circular vortex. These regions correspond to the negative core of vorticity and the region inside the isoline of maximum gradient of vorticity.

Figure 6 shows the distribution of passive particles in the negative vorticity core at successive evolutive times. For $t = 0$ the concentration distribution consists of 16 384 particles randomly distributed in a circular region corresponding to the area of negative vorticity. With this initial distribution for the passive tracers it is possible to distinguish the flow dynamics associated with the vortex core. At $t = 40$ the distribution of particles is already deformed by the elliptical vortex core. For $t = 80$ the passive tracers start to wrap around the forming satellites. This wrapping occurs due to the ejection of fluid from the core caused by its deformation, coupled with the rotation of the forming tripole. The passive tracer filament then goes on wrapping around the satellites, which is illustrated by figures 6(*c*) and 6(*d*). The rotation of the satellites causes the flow to go around the edge of the positive vorticity patches in a spiral way. Around $t = 160$ secondary structures start to form in the 2 and 8 o'clock regions of the tripole, caused by the breakup of the spiral filaments behind the satellites as they rotate clockwise. Those secondary structures are more visible for $t = 200$, figure 6(*d*), and persist afterwards. The flux of particles that exited the vortex core at the onset of the formation of the tripole ends as the core region assumes a stationary elliptical shape. At the same time, the passive tracers associated with the filaments at 2 and 8 o'clock regions of the tripole start to wrap around the secondary vortices that formed in that region. For times larger than $t = 600$ these secondary vortices are clearly defined.

Figure 7 shows the time evolution of passive particles randomly distributed inside the isoline of maximum gradient of vorticity. At $t = 0$ the passive tracer distribution consists of 16 384 particles randomly distributed inside a circular region limited by the maximum gradient of vorticity. This distribution of tracers allows us to understand if the maximum gradient of vorticity does indeed delimit the core region of the vortex (Provenzale 1999). From the evolution we can confirm that the particles that are initially inside a region very close to the isoline of maximum gradient of vorticity do stay inside the core region. Therefore, from the comparison with the evolution pictured in figure 6, it is clear that there is an initial circular region of particles that comprise the core of the vortex throughout the evolution.

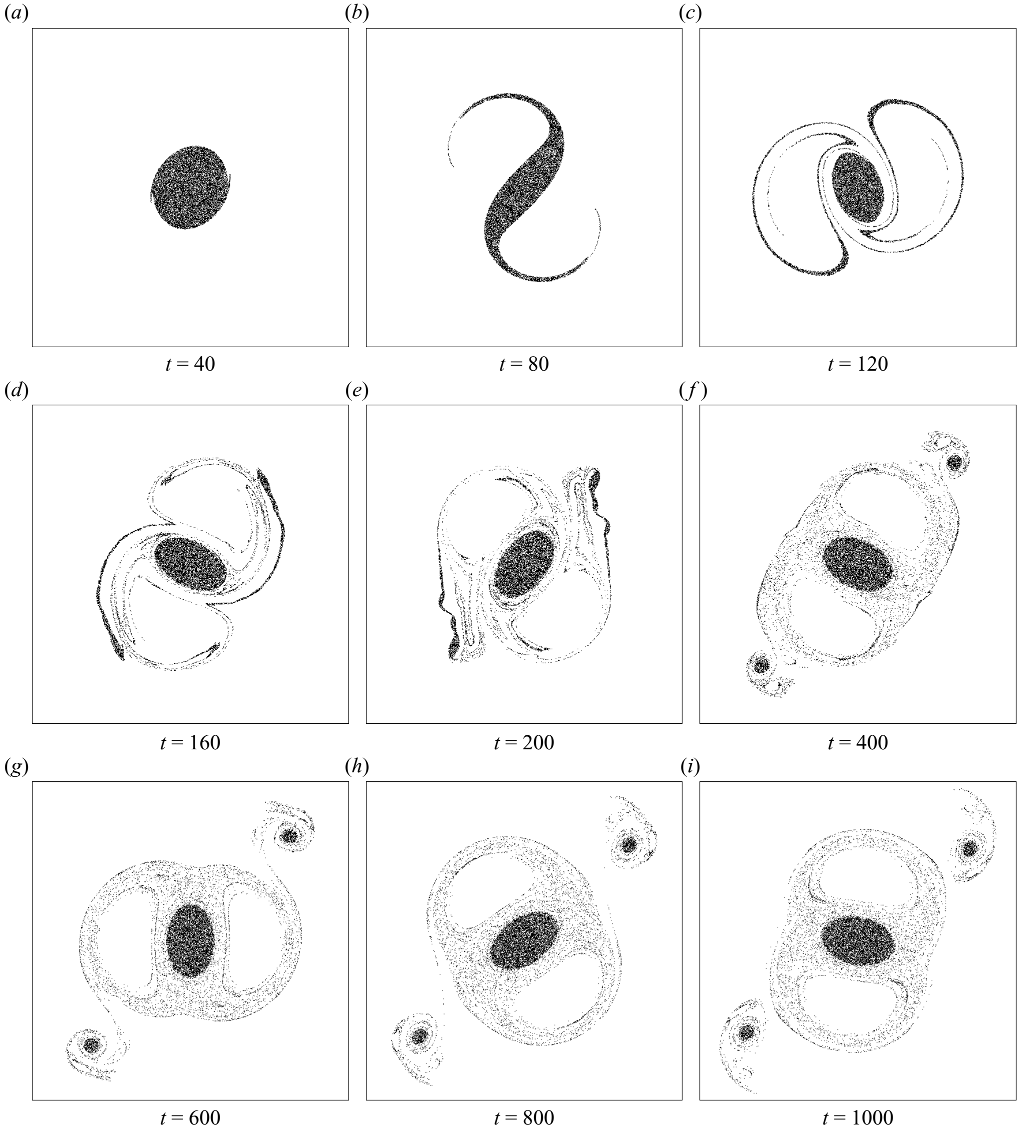

FIGURE 6. Distribution of $N = 16\,384$ passive particles initially seeded inside the core of negative vorticity.

3.3.2. *Finite-time Lyapunov exponents*

Pierrehumbert (1991) showed the importance of the study of Lyapunov exponents for the understanding of the mixing properties and chaotic behaviour of realistic flows. The main difference between vorticity and a passive tracer is that a vortex patch resists elongation and subsequential dispersal through its self-induced rotation and roll-up. On the other hand, the properties of chaotic mixing are generic and not sensitive to the details of the advecting velocity field.

Integrable systems are characterized by zero or negative Lyapunov exponents, and as a rule mixing is suppressed, while chaotic systems are characterized by positive

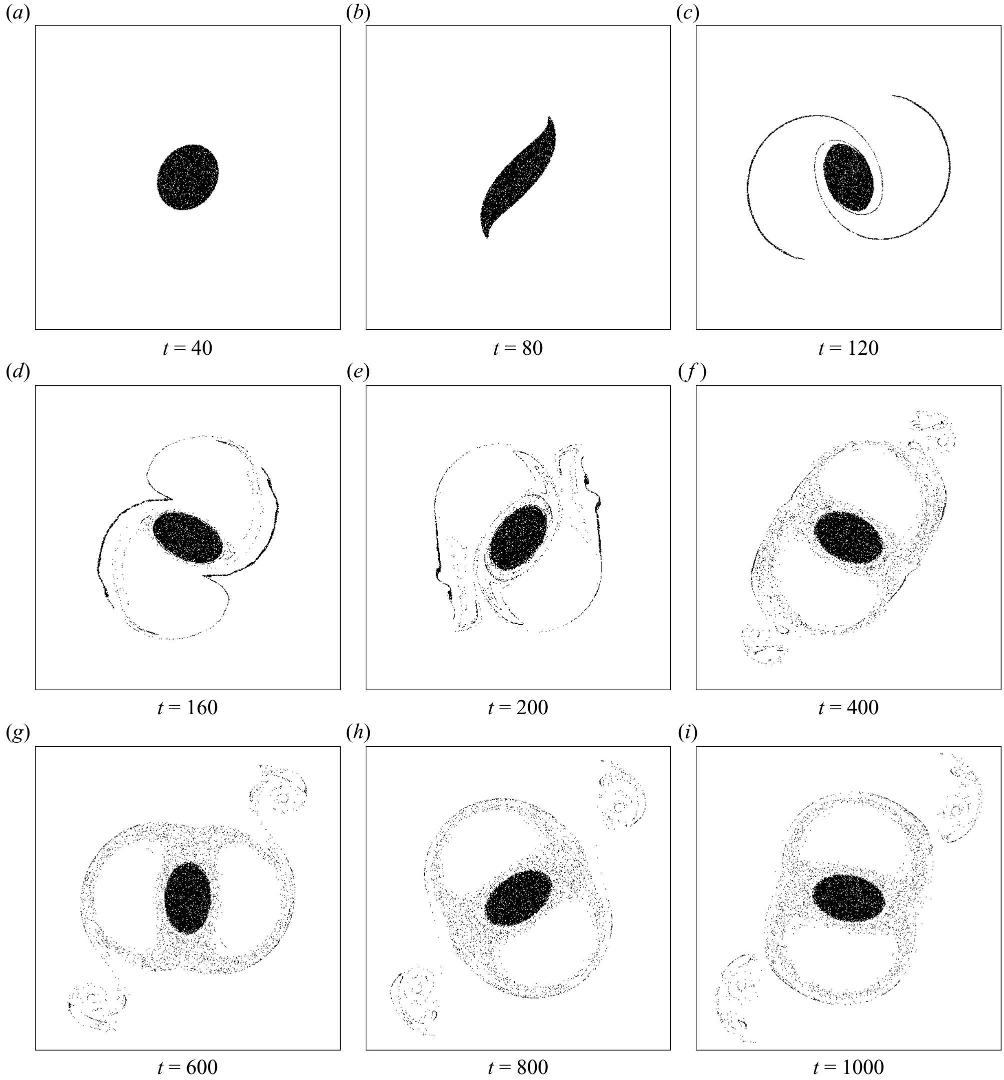

FIGURE 7. Distribution of $N = 16\,384$ passive particles initially seeded inside the inside the isoline of maximum gradient of vorticity.

Lyapunov exponents, and mixing is favoured. FTLEs analysis will be the third diagnostic method used in order to fully characterize the tripole flow.

Given an M-dimensional flow $y(t)$ generated by

$$\frac{dy_i}{dt} = F_i(\boldsymbol{y}, t), i = 1, 2, \ldots, M, \tag{3.7}$$

the Lyapunov exponent for an initial point y_0 is defined as the exponential rate of expansion of a displacement vector $\xi(t)$ which evolves according to the linearized equation of motion

$$\frac{d\xi}{dt} = \left.\frac{\partial \boldsymbol{F}}{\partial \boldsymbol{y}}\right|_{y(t)} \cdot \xi(t), \tag{3.8}$$

where $y(t)$ is the trajectory starting at y_0, $\xi(t)$ approximates the displacement between two close trajectories y_1, y_2 and $y_2 = y_1 + \xi$. Therefore, the Lyapunov exponent is given by

$$\lambda(y_0) = \lim_{t\to\infty} \frac{1}{t} \ln \frac{d(y_0, t)}{d(y_0, 0)}, \tag{3.9}$$

where $d(y_0, t) = \|\xi(y_0, t)\|$.

Because for most purposes we are interested in finite-time processes, besides the fact that in numerical calculations we cannot approach the infinite time limit, we need to work with FTLEs. The distribution of FTLEs contain much information about the topology of the region under consideration, e.g. the existence of semi-permeable barriers to transport.

An FTLE is defined by

$$\lambda(y_0, T) = \frac{1}{T} \ln \frac{d(y_0, T)}{d(y_0, 0)}. \tag{3.10}$$

For two-dimensional tracer phase sub-space, the evolution equations are defined by

$$\frac{\mathrm{d}r}{\mathrm{d}t} = \boldsymbol{V}(r, t), \tag{3.11}$$

where $\boldsymbol{V}(r, t)$ is a vector in the two-dimensional tracer phase space, the Eulerian velocity field. The corresponding linearized equation (the analogue of (3.8)) is

$$\frac{\mathrm{d}\xi}{\mathrm{d}t} = \boldsymbol{J}(t) \cdot \xi(t), \tag{3.12}$$

where $\xi(t) = ((x_2 - x_1)(t), (y_2 - y_1)(t))$ and $\boldsymbol{J} = (\partial \boldsymbol{V}/\partial r)|_{r(t)}$. In this sub-space it is possible to introduce the mean exponential rate of divergence, or tracer Lyapunov exponent, for two trajectories that are initially close in the same way as we did for (3.9):

$$\lambda(r_0) = \lim_{t\to\infty} \frac{1}{t} \ln \frac{d(r_0, t)}{d(r_0, 0)}. \tag{3.13}$$

Notice that we measure distances $d(r_0, t)$ only with respect to tracer variables. We have Lagrangian chaos when initially close trajectories diverge exponentially fast. This notion is quantified by saying that the Lyapunov exponent defined by (3.13) is positive. Defining $d(r_0, t)$ as above and plotting $H(r_0, t) = \ln(d(r_0, t)/d(r_0, 0))$ versus time, we can evaluate the FTLE as the time-dependent slope of the curve $H(r_0, t)$. Therefore, the FTLE in two-dimensional tracer sub-space is

$$\lambda(r_0, T) = \frac{1}{T} \ln \frac{d(r_0, T)}{d(r_0, 0)}. \tag{3.14}$$

3.3.3. *Distribution of Lyapunov exponents*

The procedure used to calculate the FTLEs is similar to the one used by Pierrehumbert (1991). We consider an initial Cartesian grid of 128 × 128 particles centred on the vortex centre. For each point in the initial grid, a randomly placed adjoining point is generated that is within a small distance δ. The position of the particles is recorded at several times of the evolution and the corresponding distance between close trajectories $\ln(d(r_0, t)$ is calculated. When the distance between adjoining particles becomes too large, the position of the adjoining particle is re-initialized to the original distance, so as to keep the trajectories near each other, as required by the definition of the Lyapunov exponent. The total number of these deflation factors

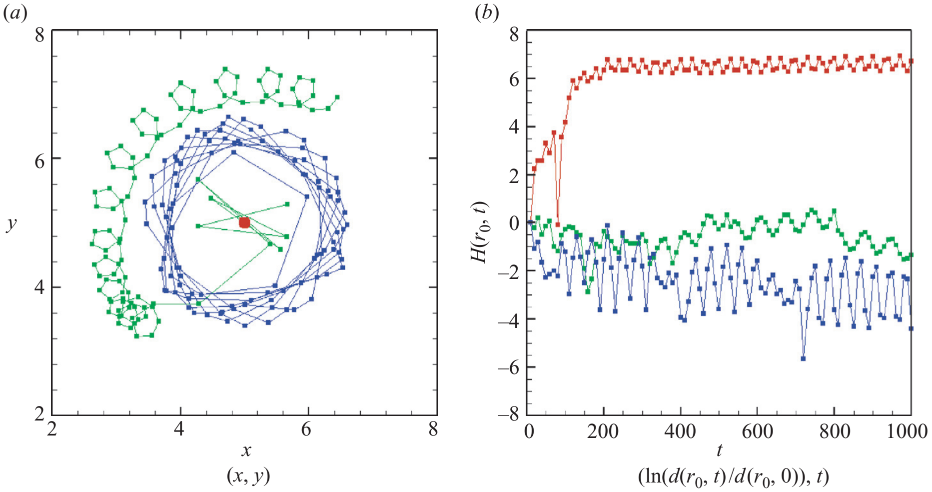

FIGURE 8. Graphs of position versus time and $H(r_0, t) = \ln(d(r_0, t)/d(r_0, 0))$ versus time for three different tracers that at $t = 0$ were at different radius from the vortex centre. Tracer 1 (red): $r(t = 0) = 0.033$. Tracer 2 (green): $r(t = 0) = 0.702$. Tracer 3 (blue): $r(t = 0) = 1.169$.

is kept track of and factored in the calculation of H. In order to have finite-time estimates of the Lyapunov exponent for several phases of the evolution, a careful choice of the time period T for which the FTLEs are calculated needs to be made. As can be expected, the choice of integration time is dependent on the particular application. The time period T needs to be short enough to be representative of the stage of the flow evolution and large enough to have well defined regions with the same FTLEs. Several integration times were used and it was found that using $T = 10$ gives a good compromise between representation of the several stages of the evolution and definition of the regular and chaotic regions.

In order to illustrate the procedure used to calculate the FTLEs, figure 8 shows the temporal evolution of the position and $H(r_0, t) = \ln(d(r_0, t)/\ d(r_0, 0))$, for three different tracers. The tracers were chosen at different positions inside the initial vortex. Tracer 1 was initially near the vortex centre, at $r = 0.033$, Tracer 2 was at $r = 0.702$, near the zone of maximum tangential velocity and finally Tracer 3 was in the ring of positive vorticity, at $r = 1.169$. Figure 8(*a*) shows snapshots of the position of the tracers at a time interval of $T = 10$ and the lines connecting the position markers are merely to serve as a guide to understand the evolution. Figure 8(*b*) shows the temporal evolution of $H(r_0, t) = \ln(d(r_0, t)/d(r_0, 0))$ for the same time interval.

Figure 9 shows snapshots of the tracer cloud for different times of the evolution. Each particle is coloured according to the respective FTLE. The FTLEs were divided in 10 levels, with bright red corresponding to high stretching ($\lambda(r_0) > 0.2$). Particles with ($\lambda(r_0) < 0.01$) were not represented. We chose to represent the FTLE for each particle at the end of the time interval. This corresponds to effectively taking snapshots of the particles at particular intervals, revealing the value of the FTLE for that time interval. When we are doing this, we are leaving out the information regarding the time history, during the particular time interval, of the particle trajectories and the evolution of the separation between two initially close trajectories during the time interval. Therefore, it is not possible to distinguish in the same region of similar FTLE how the particles/trajectories reached that particular value for their FTLE.

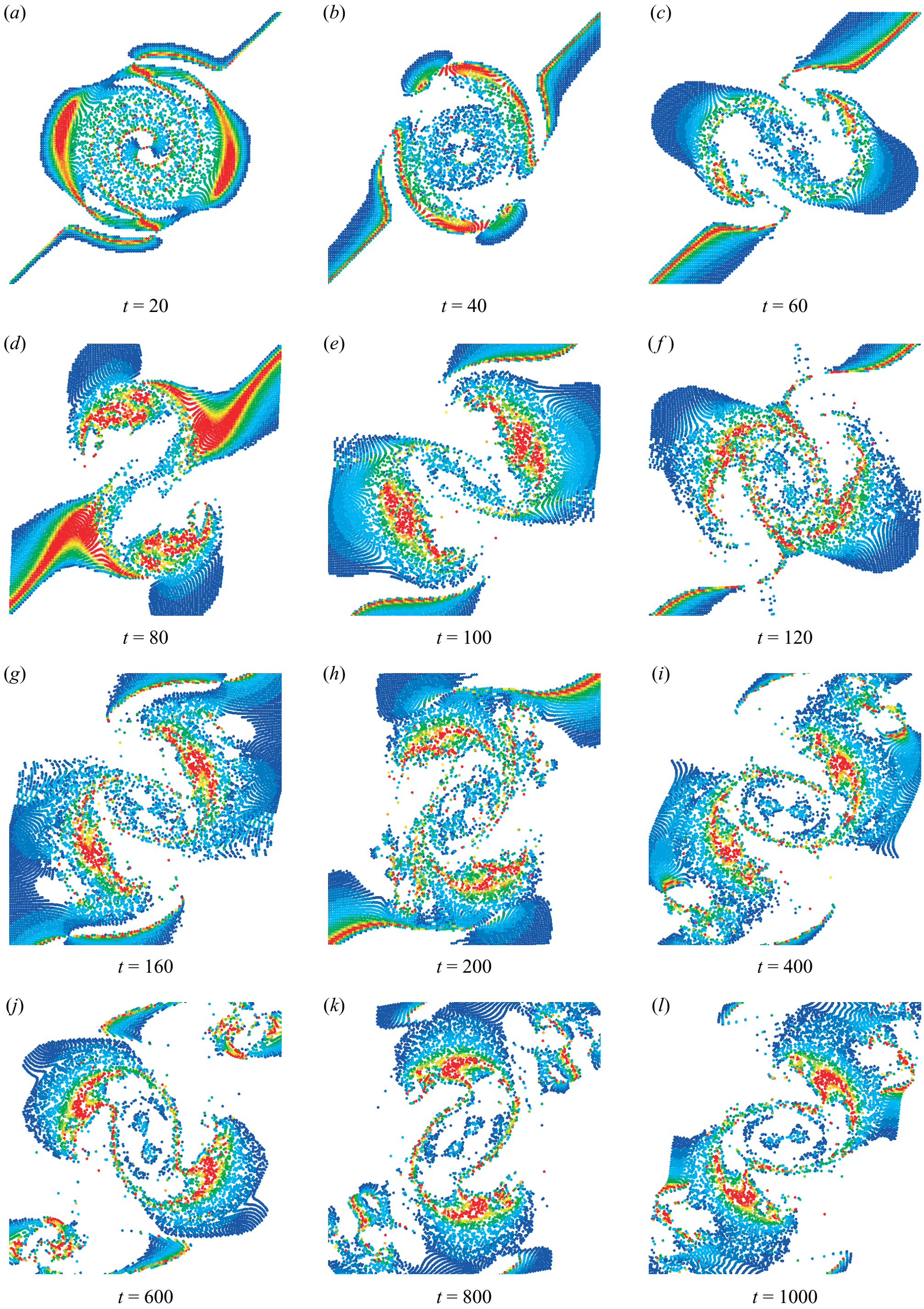

(*a*) $t = 20$

(*b*) $t = 40$

(*c*) $t = 60$

(*d*) $t = 80$

(*e*) $t = 100$

(*f*) $t = 120$

(*g*) $t = 160$

(*h*) $t = 200$

(*i*) $t = 400$

(*j*) $t = 600$

(*k*) $t = 800$

(*l*) $t = 1000$

FIGURE 9. Snapshots of the tracer cloud at various times. Particles have been colour-coded by the corresponding FTLE. Red is for high stretching and blue is for low stretching.

This analysis can distinguish chaotic regions from regions of invariant tori, as the former are characterized by positive exponents. Furthermore, it is possible to identify non-communicating chaotic bands, as each of these regions will be characterized by a different Lyapunov exponent. In this analysis, the term regular (flow) is used as opposed to chaotic flow, and is measured using the corresponding FTLE.

As would be expected, the formation of the tripole is characterized by high levels of stretching. As the perturbation grows, two spiral regions of high-stretching develop, and can be seen for $t = 20$. As these spirals develop, invariant tori are trapped inside the chaotic regions, figure 9(*b*). At the same time, the core is composed of two distinct regions, with one of the regions remaining regular while the rest of the core is characterized by low stretching. As the tripole forms, with the vortex core breaking through the ring of positive vorticity and the satellites starting to form, two large regions of regular flow, divided by a region of chaotic flow, form for each satellite. These regions are visible in figures 9(*c*) and 9(*d*). With the formation of the satellites, it is clear that their structure is made of regions of invariant tori divided by regions of chaotic flow, that evolve in a spiral way. This is interesting, because it shows that the satellites are not only formed through one regular structure issuing from the breaking up of the outer ring of positive vorticity. The core on the other hand is composed of macroscopic islands of regular and low-stretching flow. Looking at figure 9(*e*), when the tripole is being formed, it is clear that the poles of positive vorticity largely correspond to regular regions. Regions of high-stretching near the 'leading edge' of the positive vorticity poles occur both inside the pole and in the region that in the vorticity plot is between the pole of positive vorticity and the outer filament of negative vorticity. It is also clear that the core region is composed of low-stretching regions along with regular regions.

For $t = 120$ the tripole is fully formed. From figure 9(*f*) it is clear that the tripole is formed around distinct and largely regular regions, corresponding to the core of negative vorticity and the two satellites of positive vorticity. However, for longer times of the fully formed tripolar vortex, figures 9(*i*) to 9(*l*), regions of high-stretching still persist at the 'leading edge' of the poles of positive vorticity, and the core of negative vorticity is surrounded by barriers of medium-to-high stretching.

The regions of regular flow that form the vorticity poles are regions where transport is suppressed, with transport occurring mainly in the regions of chaotic flow that surround the tripolar vortex after its formation. However, not only the chaotic regions of the flow act as transport barriers, the vorticity gradient also represents a transport barrier. That is obvious when comparing the plots for vorticity, concentration, randomly distributed particles and Lyapunov exponents, e.g. for $t = 80$. By looking at figure 9(*d*), we can see that the particles that are exiting the stretched out core have both regular regions and medium-stretching regions. However, there are clear barriers of transport to this flow of particles that occur in regions of regular or low stretching. Those regions correspond to ridges of maximum vorticity gradient. As the tripolar vortex is formed, the flow that exits the vortex core after it breaks the outer ring of positive vorticity is composed of both chaotic and regular regions that are contained by lines of maximum vorticity gradient. As the tripolar vortex evolves, the conjugate action of maximum vorticity gradient lines and the regions of chaotic flow persists to create barriers to transport. With the regularization of the flow, the chaotic bands weaken but are still present. That is quite apparent in figures 9(*i*) through 9(*l*). As the flow reaches a degree of regularization, the existence of the above mentioned barriers to transport is responsible for maintaining the integrity of the whole tripolar system.

4. Conclusions

Mixing in two-dimensional vortex systems is a relevant subject since it occurs in many applications, from some problems in turbulence to physical problems arising in laboratory experiments and/or in nature. In this paper, the dynamics of both passive scalars and tracers in a two-dimensional flow with physical significance in a diverse number of applications, the tripolar vortex, was investigated.

The transport of passive scalars is the result of the concurrent contributions of both molecular diffusion and advection. In order to quantify the first, we looked at the scalar variance evolution and the concentration patterns for Schmidt numbers $Sc = 0.1$, 1, 10 and 100. During the formation of the tripole, an accelerated scalar dissipation is observed. That dissipation is connected to the advection-dominated processes associated with the exponential growth and subsequent halt of the perturbation mode. This stage of accelerated dissipation is preceded and followed by stages of diffusion-dominated scalar dissipation. However, these two mainly diffusive stages have different evolutions for the results with the same Schmidt number, translated into different slopes of the scalar variance curve. For Schmidt numbers greater than 10 the scalar variance evolution is virtually the same, indicating that in order to simulate the behaviour of scalars with high Sc numbers it is enough to simulate lower values of this parameter.

The evolution of the concentration spatial distribution for three of the four studied scalars allowed us to identify the differences between the mixing of different passive scalars and vorticity. Through the placing of the concentration patch in the core region of negative vorticity, it is possible to qualitatively distinguish the flow pattern differences between the passive scalar concentration and the active scalar vorticity. These differences occur mainly during the two diffusive stages of the tripolar vortex evolution. During the formation of the tripole, which is a process dominated by strong advection, the patterns of mixing of the different passive scalars are very much the same as for vorticity. The evolution of the scalar concentration spatial distribution shows as well that throughout the evolution, barriers to transport exist that limit passive scalar dispersion.

In order to help us understand the role that the core dynamics play in the formation of the whole tripole system, the dynamics of randomly distributed passive particles was studied. Particles were placed in two different regions of the initial circular vortex, corresponding to the negative core of vorticity and the region inside the isoline of maximum gradient of vorticity. The fact that the particles that are initially inside a region very close to the isoline of maximum gradient of vorticity stay inside that region shows that the line maximum gradient of vorticity acts as a barrier to transport.

One way of identifying barriers to mixing, and perhaps more importantly regions of chaotic mixing, is to make use of FTLEs. Patterns of the temporal evolution of FTLEs, for a Cartesian grid of particles centred on the vortex centre at the start of the evolution, were examined. It is shown that, as the perturbation seeded in the initial flow grows and the tripolar vortex is formed, two large regions of regular flow, divided by a region of chaotic flow, form for each satellite, showing that they are not simply formed through one regular structure issuing from the breaking up of the outer ring of positive vorticity. The core, however, is composed of regions of regular or low-stretching flow. When the tripole is fully formed, it is composed of three distinct largely regular regions, corresponding to the core of negative vorticity and the two satellites of positive vorticity. However, high-stretching regions still persist at the ‘leading edge’ of the satellites, as well as regions of low-to-medium stretching around the negative vorticity core.

When comparing the contour plots for vorticity, concentration, randomly distributed particles and Lyapunov exponents, it is apparent that transport barriers exist along lines of maximum vorticity gradient. This is especially noticeable during the formation of the tripolar vortex. However, from the evolution of FTLEs it can be seen that regular regions surrounded by chaotic bands are also responsible for some barriers to transport during the tripole formation and subsequent permanence. For longer times, even though the levels of stretching are lower and vorticity gradients are less pronounced, these two factors are still responsible for the integrity of the tripolar system.

The first author would like to acknowledge the support of FCT (SFRH/BD/1129/2000 and SFRH/BPD/21778/2005). The authors would also like to thank one anonymous reviewer for his comments, which have greatly improved the original manuscript.

REFERENCES

Abraham, E. R. & Bowen, M. M. 2002 Chaotic stirring by a mesoscale surface-ocean flow. *Chaos* **12**, 373–381.

Babiano, A., Basdevant, C., Legras, B. & Sadourny, R. 1987 Vorticity and passive scalar dynamics in two-dimensional turbulence. *J. Fluid Mech.* **183**, 379–397.

Bajer, K., Bassom, A. P. & Gilbert, A. D. 2001 Accelerated diffusion in the centre of a vortex. *J. Fluid Mech.* **437**, 395–411.

Bassom, A. P. & Gilbert, A. D. 1998 The spiral wind-up of vorticity in an inviscid planar vortex. *J. Fluid Mech.* **371**, 109–140.

Bassom, A. P. & Gilbert, A. D. 1999 The spiral wind-up and dissipation of vorticity and a passive scalar in a strained planar vortex. *J. Fluid Mech.* **398**, 245–270.

Boatto, S. & Pierrehumbert, R. T. 1999 Dynamics of a passive tracer in a velocity field of identical point vortices. *J. Fluid Mech.* **394**, 137–174.

Bogucki, D., Domaradzki, J. A. & Yeung, P. K. 1997 Direct numerical simulations of passive scalars with $Pr > 1$ advected by turbulent flow. *J. Fluid Mech.* **343**, 111–130.

Carton, X., Flierl, G. R. & Polvani, L. 1989 The generation of tripoles from unstable axisymmetric isolated vortex structures. *Europhys. Lett.* **9**, 339–344.

Elhmaidi, D., Provenzale, A., Lili, T. & Babiano, A. 2004 Stability of two-dimensional vorticity filaments. *Phys. Fluids* A **333**, 85–90.

Ferreira de Sousa, P. J. S. A. & Pereira, J. C. F. 2005 Fourth and tenth order compact finite difference solutions of perturbed circular vortex flows. *Intl J. Numer. Fluids* **49**, 603–618.

Flohr, P. & Vassilicos, J. C. 1997 Accelerated scalar dissipation in a vortex. *J. Fluid Mech.* **348**, 295–317.

Fuentes, O. U. V., van Heijst, G. J. F. & van Lipzig, N. P. M. 1996 Unsteady behaviour of a topography-modulated tripole. *J. Fluid Mech.* **307**, 11–41.

von Hardenberg, J., McWilliams, J. C., Provenzale, A., Shchepetkin, A. & Weiss, J. B. 2000 Vortex merging in quasi-geostrophic flows. *J. Fluid Mech.* **412**, 331–353.

van Heijst, G. J. F. & Kloosterziel, R. C. 1989 Tripolar vortices in a rotating fluid. *Nature* **338**, 569–571.

van Heijst, G. J. F., Kloosterziel, R. C. & Williams, C. W. M. 1991 Laboratory experiments on the tripolar vortex in a rotating fluid. *J. Fluid Mech.* **225**, 301–331.

Kevlahan, N. K.-R. & Farge, M. 1997 Vorticity filaments in two-dimensional turbulence: creation, stability and effect. *J. Fluid Mech.* **346**, 49–76.

Kloosterziel, R. C. & Carnevale, G. F. 1999 On the evolution and saturation of instabilities of two-dimensional isolated circular vortices. *J. Fluid Mech.* **388**, 217–257.

Kuznetsov, L. & Zaslavsky, G. M. 1998 Regular and chaotic advection in the flow field of a three-vortex system. *Phys. Rev.* E **58**, 7330–7349.

Kuznetsov, L. & Zaslavsky, G. M. 2000 Passive particle transport in three-vortex flow. *Phys. Rev.* E **61**, 3777–3792.

Lapeyre, G. 2002 Characterization of finite-time Lyapunov exponents and vectors in two-dimensional turbulence. *Chaos* **5**, 688–698.

Legras, B., Santangelo, P. & Benzi, R. 1988 High-resolution numerical experiments for forced two-dimensional turbulence. *Europhys. Lett.* **5**, 37–42.

Leith, C. E. 1984 Minimum enstrophy vortices. *Phys. Fluids* **27**, 1388–1395.

Lele, S. K. 1992 Compact finite difference schemes with spectral-like resolution. *J. Comput. Phys.* **103**, 16–42. *J. Fluid Mech.* **346**, 49–76.

Meunier, P. & Villermaux, E. 2003 How vortices mix. *J. Fluid Mech.* **476**, 213–222.

Ottino, J. M. 1990 Mixing, chaotic advection, and turbulence. *Annu. Rev. Fluid Mech.* **22**, 207–254.

Pierrehumbert, R. T. 1991 Large-scale horizontal mixing in planetary atmospheres. *Phys. Fluids* A **3**, 1250–1260.

Pierrehumbert, R. T. & Yang, H. 1993 Global chaotic mixing on isentropic surfaces. *J. Atmos. Sci.* **50**, 2462–2480.

Pingree, R. D. & LeCann, B. 1992 Anticyclonic eddy x91 in the southern bay of Biscay, May 1991 to February 1992. *J. Geophys. Res.* **97**, 14353–14367.

Provenzale, A. 1999 Transport by coherent barotropic vortices. *Annu. Rev. Fluid Mech.* **31**, 55–93.

Rhines, P. B. & Young, W. R. 1983 How rapidly is a passive scalar mixed within closed streamlines. *J. Fluid Mech.* **133**, 133–145.

Rossi, L. F., Lingevitch, L. F. & Bernoff, A. J. 1997 Quasi-steady monopole and tripole attractors in relaxing vortices. *Phys. Fluids* **9**, 2329–2338.

Vranjes, J. 1999 Tripolar vortex in plasma flow. *Planet. Space Sci.* **47**, 1531–1535.

Vranjes, J., Maric, G. & Shukla, P. K. 1999*a* Tripolar vortices and vortex chains in dusty plasma *Phys. Lett.* A **258**, 317–322.

Vranjes, J., Stenflo, L. & Shukla, P. K. 1999*b* Tripolar vortices and vortex chains in a shallow atmosphere. *Phys. Lett.* A **267**, 184–187.

Warhaft, Z. 2000 Passive scalars in turbulent flows. *Annu. Rev. Fluid Mech.* **32**, 203–240.

Waugh, D., Abraham, E. R. & Bowen, M. M. 2006 Spatial variations of stirring in the surface ocean: a case study of the Tasman sea. *J. Phys. Oceanogr.* **36**, 526–542.

Wonhas, A. & Vassilicos, J. C. 2001 Mixing in frozen and time-periodic two-dimensional vortical flows. *J. Fluid Mech.* **442**, 359–385.

Yeung, P. K. 2002 Lagrangian investigations of turbulence. *Annu. Rev. Fluid Mech.* **34**, 115–142.